Journal of Materials Chemistry A

Accepted Manuscript

ROYAL SOCIETY OF CHEMISTRY

www.rsc.org/materialsA

Journal Name

ARTICLE

Glucose-derived nitrogen-doped hierarchical hollow nest-like carbon nanostructure from a novel template-free method as an outstanding electrode material for supercapacitors

Received 00th January 20xx,
Accepted 00th January 20xx

DOI: 10.1039/x0xx00000x

www.rsc.org/

Ji-Yuan Liang, Chun-Chieh Wang, Shih-Yuan Lu*

Nitrogen-doped hierarchical hollow nest-like carbon (NHHNC) nanostructure was fabricated from glucose with a novel template-free method. A hollow nest-like precursor, $Ni(OH)_2$@N-polysaccharide, was first formed through a hydrothermal treatment of glucose in the presence of $NiSO_4$ and hexamethylenetetramine (HMT), with glucose serving as the carbon source, HMT as the precipitant and nitrogen source, and $NiSO_4$ as the main structure-directing reagent. The hierarchical porous carbon structure was created through thermal carbonization and activation followed by acid etching, of the hollow nest-like precursor. The NHHNC was a hierarchical porous structure composed of three-dimensionally intercepting N-doped porous carbon sheets and possessed micropores, mesopores, and macropores. This unique hierarchical hollow nest-like porous structure is ideal for applications as electrodes for supercapacitors, with the micropores offering large surface areas to accommodate electric double layer capacitances, the mesopores as fast ion transport channels, and the macropores as the electrolyte reservoir for fast ion supply. These advantageous structural features, together with the fast charge transport ability of the partially graphitized carbon sheets and extra pseudocapacitances generated through superficial redox reactions of the N-doped sites, led to outstanding capacitive performances of the NHHNC. The NHHNC electrode exhibited a high specific capacitance of 322 F g^{-1} at 1 A g^{-1}, an excellent high rate capability of 54% capacitance retention at 20 A g^{-1}, and an outstanding cycling stability of only 2% loss in specific capacitance after 10,000 cycles at a current density of 10 A g^{-1}, among the best reported. The present template-free process however, unlike the often cumbersome templating ones, is well suited for mass production and thus practical applications.

1. Introduction

Energy management is a critical part of the green energy infrastructure that is essential for the everlasting development of mankind. Supercapacitors (also called electrochemical capacitors), as a key player in energy management, have drawn intensive and extensive research attentions in the past couple of decades, because of their high power densities, fast charging/discharging time, long cycle life, and high reliability. They can offer both electric double-layer capacitances (EDLCs) and pseudo-capacitances depending on the kind of electrode materials used.[1] Metal oxides and conducting polymers generate pseudo-capacitances through superficial redox reactions, while carbonaceous materials produce EDLCs via physical sorption/desorption of counter-balanced ions.[2-5]

Carbonaceous materials continue to be the most widely used electrode material for supercapacitors because of their high surface areas, outstanding chemical stability, and low cost. One of the key issues associated with carbon based supercapacitors is the further improvement of specific capacitances to boost their energy densities.[6] One way to achieve this goal is to dope heteroatoms, such as O, N, B, and S, into the carbon electrodes, with which the electrode offers not only EDLCs but also pseudocapacitances through the superficial redox reactions of the doped heteroatoms with the electrolyte.[7-12] Among the many investigated doped carbon materials, nitrogen-doped carbons have recently drawn a great deal of research attention.[13] Nitrogen-doped carbons can be prepared by post-treatment of the pristine carbon with ammonia, urea, or pyridine to introduce nitrogen-containing groups onto the surfaces of the pristine carbon.[14,15] Another method is direct thermal carbonization of nitrogen-containing polymer precursors, such as polyacrylonitrile,[16] polyaniline,[17] polypyrrole,[18] and melamine resin.[19]

In addition to capacitances, electrode kinetics, especially high rate capability, is also an essential factor to consider for designing an outstanding supercapacitor electrode for practical applications. It is well known that microstructure plays a key role in determining the capacitive performances of the electrode. For one example, activated carbons have been one of the most common porous carbon materials for applications in supercapacitors as the electrode material. They usually exhibit high specific capacitances at low current densities because of

Department of Chemical Engineering, National Tsing Hua University, Hsinchu 30013, Taiwan
E-mail address: sylu@mx.nthu.edu.tw
Electronic Supplementary Information (ESI) available: See DOI:10.1039/x0xx00000x

their high surface areas for accommodation of EDLCs, but suffer from the poor electrode kinetics at high current densities, because of the large mass transfer resistances of the electrolyte ions in the narrow inner pores of the material. In recent years, three dimensional (3-D) hierarchical porous carbon materials that possess not only micropores but also mesopores and macropores, have received a great deal of research attention. This unique carbon structure is ideal for applications as electrode materials in supercapacitors, with the micropores offering large surface areas to accommodate electric double layer capacitances, the mesopores as fast ion transport channels,[20,21] and the macropores as the electrolyte reservoir for fast ion supply.[22-24] Most of the 3-D hierarchical carbon structure was fabricated with templating methods, by using inorganic matrices (for example, self-assembled SiO_2 spheres) and/or surfactant-derived soft templates (for example, block copolymers) for creation of the hierarchical pore structure.[25-28] For example, Wen et al. fabricated hierarchical porous carbons with a colloidal SiO_2 crystal as the macropore template and triblock copolymers as the mesopore template. The fabrication procedures involved self-assembly of uniform sized SiO_2 spheres, impregnation of carbon precursor into the ordered SiO_2 crystal, and carbonization and removal of the template.[29] Evidently, the fabrication process of the templating method is cumbersome, and thus not feasible for large scale production. Consequently, template-free methods should be developed to provide a more facile and scalable way for fabrication of hierarchical carbon structures.

With the above analysis, one concludes that heteroatom-doped hierarchical porous carbon structure fabricated with a template-free method, may serve as a scalable, cost-effective high performance supercapacitor electrode material. In this work, we developed a novel template-free method to produce nitrogen-doped hierarchical hollow nest-like carbon (NHHNC) structure from glucose. As shown in Scheme 1, a hollow nest-like precursor, $Ni(OH)_2$@N-polysaccharide, was first created through a hydrothermal treatment of glucose in the presence of $NiSO_4$ and hexamethylenetetramine (HMT), with glucose serving as the carbon source, HMT as the precipitant and nitrogen source, and $NiSO_4$ as the main structure-directing reagent. The hierarchical porous carbon structure was created through thermal carbonization and activation followed by acid etching, of the hollow nest-like precursor. During the thermal carbonization and activation process, $ZnCl_2$ was introduced to facilitate the formation of micropores and graphitization of the carbon sheets. The $Ni(OH)_2$@N-polysaccharide precursor was converted into $Ni_3ZnC_{0.7}$/Ni composite nanocrystals coated carbon structure, $Ni_3ZnC_{0.7}$/Ni@C. The $Ni_3ZnC_{0.7}$/Ni composite nanocrystals were then removed with HCl etching, leaving behind mesopores on the carbon sheets. The morphology of the nest-like structure remained the same throughout the whole process to give the NHHNC. This hierarchical hollow nest-like carbon material contained micropores, mesopores, and macropores, and was investigated its capacitive performances as a supercapacitor electrode. The NHHNC electrode exhibited a high specific capacitance of 322 F g^{-1} at 1 A g^{-1}, an excellent high rate capability of 54% capacitance retention at 20 A g^{-1}, and an outstanding cycling stability of only 2% loss in specific capacitance after 10000 cycles at a current density of 10 A g^{-1}, among the best reported. The present facile and template-free fabrication method sheds a new light on the scalable production of nitrogen-doped hierarchical porous carbon materials of well-defined morphology for electrode applications.

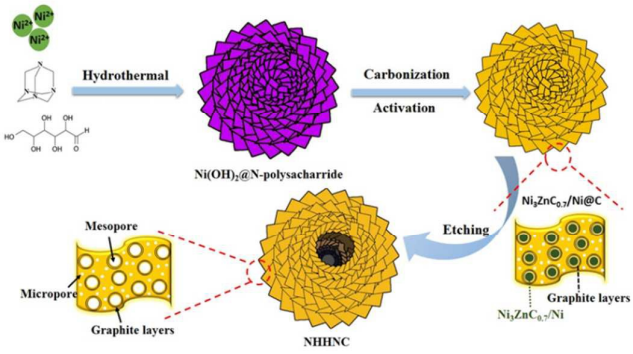

Scheme 1 Schematic illustration of nitrogen-doped hierarchical hollow nest-like carbon formation

2. Experimental

2.1 Materials

Nickel sulfate hexahydrate ($NiSO_4 \cdot 6H_2O$), hexamethylenetetramine, zinc chloride ($ZnCl_2$), glucose ($C_6H_{12}O_6$), and all other chemicals used in this study are analytical grade and were used without further purification.

2.2 Synthesis of nest-like $Ni(OH)_2$@N-polysaccharide composite

Firstly, 1.31 g of $NiSO_4 \cdot 6H_2O$, 0.7 g of HMT, and 0.7 g of glucose were dissolved in 40 mL distilled water with magnetic stirring at room temperature for 10 min to obtain a uniform solution. The solution was then transferred to and sealed in a 50 mL teflon-lined autoclave, heated to 180 ^oC and maintained at that temperature for 24 h. The solid product was collected with a centrifuge and washed several times with distilled water until the pH value of the supernatant was about 7. The rinsed product was further dried at 80 ^oC for 12 h in an oven to afford the final product.

2.3 Synthesis of nitrogen-doped hierarchical hollow nest-like carbon

Firstly, the $Ni(OH)_2$@polysaccharide composite and $ZnCl_2$ were mixed together at a mass ratio of 2:1. The mixture was then loaded into a ceramic boat to be calcined in a tubular furnace at 700 ^oC in a N_2 atmosphere for 3 h. The heating rate was 5 ^oC min^{-1}. Black powders were obtained after the calcination. Here, the calcination operation was conducted to carbonize the $Ni(OH)_2$@polysaccharide composite. $ZnCl_2$ served as an enhancing compound for both the activation and graphitization of the carbon structure formed during the carbonization operation.

These black powders were further suspended in a 37% HCl solution for a hydrothermal treatment at 180 ^oC for 24 h to remove the metallic constituents, Ni and Zn, from the product. The solid product was collected with a centrifuge, rinsed with distilled water for several times, and dried at 80 ^oC to afford the final product, the nitrogen-doped hierarchical hollow nest-like carbon, NHHNC. For comparison purpose, we also prepared nitrogen-doped hierarchical hollow nest-like carbon without activation, termed NHHNC-na. The procedures were the same with those of the NHHNC except that no $ZnCl_2$ was added during the calcination.

For further comparison, we prepared plain carbonaceous products without the involvement of $NiSO_4 \cdot 6H_2O$, HMT, $ZnCl_2$, and HCl. Briefly, 1.4 g of glucose was dissolved in 40 mL distilled water for the hydrothermal treatment, followed by calcination at 700 °C in a N_2 atmosphere for 3 h. The product appeared as spherical particles of carbon, and was termed carbon sphere in this study.

2.4 Characterization

A scanning electron microscope (SEM, Hitachi S-4800) and a transmission electron microscope (TEM, JEOL JEM-2011) were used for morphology observation of the samples. X-ray diffraction measurements (XRD, Philips, X'pert pro) was conducted to characterize the crystalline structure of the samples. Fourier transform infrared (FTIR) spectra were recorded on a Perkin–Elmer spectrophotometer to gain bonding information of the samples. Thermogravimetric (TG) analysis was performed on a thermogravimetric analyzer (TA Instruments Q50) at a heating rate of 2 °C min^{-1} under air atmosphere to confirm the removal of metallic constituents of the products. Nitrogen adsorption-desorption isotherms were obtained with a gas adsorption analyzer (ASAP 2020, Micromeritics Instrument Co. USA) at 77 K to characterize the microstructure of the products. X-ray photoelectron spectroscopy (XPS) was conducted on a ULVAC-PHI X-ray photoelectron spectrometer, using Mg Kα (1253.6 eV) radiation from a double anode at 150 W, to identify the surface composition of the samples.

2.5 Electrochemical measurements

All electrochemical experiments were carried out on a CHI 660D electrochemical workstation. The working electrodes were prepared as follows: a mixture containing 85 wt.% of active materials, 10 wt.% of acetylene black, and 5 wt.% poly(vinylidene fluoride) was prepared, and then the mixture was suspended in 20 μL 1-methyl-2-pyrrolidone, with ultrasound agitation for 30 min. The product was dropped onto a graphite substrate (10 × 10 × 3 mm) that serves as a current collector and then dried at 80 °C in an oven overnight. The electrolyte used was 6 M KOH aqueous solution. A Pt wire and an Hg/HgO electrode were used as counter and reference electrodes, respectively. The electrochemical impedance spectroscopy was carried out at open circuit potential with a sinusoidal signal over a frequency range from 100 kHz to 10 mHz at an amplitude of 10 mV.

3. Results and discussion

The morphologies of the intermediate and final products were characterized with SEM and HRTEM. Figure 1a shows a typical SEM image of the hollow nest-like precursor, $Ni(OH)_2$@N-polysaccharide. It appears as aggregates of particles of several μm in diameter, with the particle surface being a network of intercepting sheets, which we refer to as a nest-like structure. This nest-like structure can be more clearly observed from the inset, a locally enlarged SEM image. The morphology of the precursor after thermal carbonization and activation, as shown in Fig. S1, remained unchanged. The nest-like structure continued to remain even after the acid etching treatment, as depicted in Figure 1b, for the final product. Interestingly, these nest-like particles were hollow with a thickness of several hundred nanometers as revealed by some broken nest-like particles.

Fig. 1c shows an HRTEM image of a nest-like particle of the final product. The hollow structure of the particle was revealed as the inner lighter region of the image, with the outer darker region being the shell of the hollow structure. The inset shows a thin sheet located at the outer most region of the nest-like particle. If examined closely, the thin sheet is full of pores. Fig. 1d shows the further enlarged HRTEM image of the thin sheet, from which there can be identified pores of sizes ranging from about 4 to 25 nm in dimension. These pores are surrounded by thin crystalline layers, whose inter-layer distances can be measured to be 0.34 nm, in good agreement with the *d*-spacing of graphite in the [001] direction.[30] Furthermore, there can also be identified voids of around 4 nm in size within the graphite layers, highlighted with red dotted circles. These voids are structural defects of the graphitic lattices. One thus can conclude that the final product is composed of hollow nest-like particles, with the shells being constructed from intercepting porous, partially graphited carbon sheets.

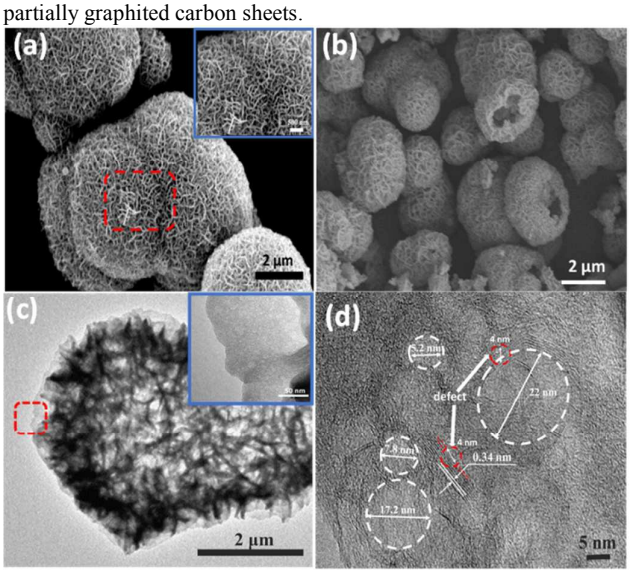

Fig. 1 (a) SEM of $Ni(OH)_2$@N-polysaccharide, (b) SEM of NHHNC, (c) HRTEM image of NHHNC and (d) locally enlarged HRTEM images of carbon sheet of NHHNC. Inset of (a) shows zoom-in SEM image of precursor. Inset of (c) shows locally enlarged HRTEM image of carbon sheet edge.

The intermediate and final products were further investigated their crystalline structure and composition with XRD characterizations. Fig. 2 shows the XRD patterns obtained for the products after the hydrothermal treatment and after the thermal carbonization and activation treatments, and also the final product. First, the diffraction peaks of the hydrothermal product can be assigned to those of $Ni(OH)_2$ (JCPDS #38-0715) and the product is proposed to be a $Ni(OH)_2$/N-polysaccharide composite. The formation mechanism is proposed as follows. The hydrolysis of HMT produces hydroxide ions (OH^-) and amine ions (NH_4^+) in the solution (Eq. (1)).[31] The Ni^{2+} from $NiSO_4$ then reacts with OH^- to form $Ni(OH)_2$ (Eq. (2)).

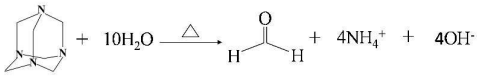

(1)

(2)

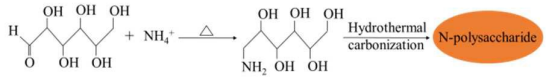

(3)

In the meantime, the aldehyde group of glucose reacts with NH_4^+ to form azomethine (Eq. (3)).[32] Azomethine is not stable and proceeds with the hydrothermal carbonization reaction to form N-polysaccharide.[33,34] The hydrothermal product is thus proposed to be a $Ni(OH)_2$/N-polysaccharide composite. The presence of the nitrogen containing group was confirmed with FTIR measurements. Fig. S2 shows the FTIR spectrum of the composite. The small band at around 1400 cm^{-1} can be ascribed to the C-N stretching vibration and the broad band at 3440 cm^{-1} can be attributed to the N-H stretching vibration, confirming the existence of nitrogen containing groups.[17,35] It is worth mentioning that the use of both HMT and $NiSO_4$ is essential for the formation of the nest-like structure. Without any or both of them, only micron-sized spherical particles can be obtained, as shown in Fig. S3.

The hydrothermal product, $Ni(OH)_2$/N-polysaccharide composite, was converted into $Ni_3ZnC_{0.7}$/Ni coated carbons, $Ni_3ZnC_{0.7}$/Ni@C, with the thermal carbonization and activation treatments at high temperatures. The diffraction peaks at the 2θ values of 44.5, 51.8, and 76.4° can be indexed to the (111), (200) and (220) planes, respectively, of the cubic phase of nickel (JCPDS #04-0850). Additionally, the diffraction peaks at the 2θ values of 42.8, 49.9, 73.1, and 88.5° can be indexed to the (111), (200), (220) and (311) planes, respectively, of the cubic phase of $Ni_3ZnC_{0.7}$ (JCPDS #28-0713). These results suggest that part of nickel, produced in-situ through reduction of the $Ni(OH)_2$ by carbon formed during the thermal carbonization, reacted with $ZnCl_2$ to form $Ni_3ZnC_{0.7}$, giving the $Ni_3ZnC_{0.7}$/Ni composite nanocrystals coated on the carbon sheet. This product, $Ni_3ZnC_{0.7}$/Ni@C, is magnetically responsive and can be collected with a magnet as demonstrated in Fig. S4a.

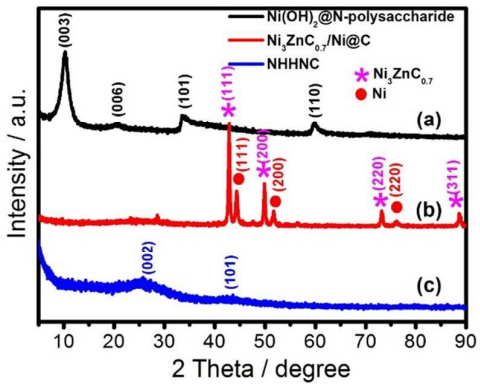

Fig. 2 XRD patterns of (a) $Ni(OH)_2$@N-polysaccharide precursor, (b) $Ni_3ZnC_{0.7}$/Ni@C composite, and (c) NHHNC.

The final product, NHHNC, was obtained by etching $Ni_3ZnC_{0.7}$/Ni@C in HCl solution to remove the metallic components. After the etching operation, the diffraction peaks associated with $Ni_3ZnC_{0.7}$ and Ni disappeared, leaving behind two broad and low-intensity diffraction peaks centering around the 2θ values of 25 and 44°, characteristic diffraction peaks of graphite of the (002) and (101) planes, respectively. This suggests that the final product contains thin graphitic crystal domains embedded in an amorphous carbon matrix.[27] It is to be noted that Ni helps catalyze the graphitization of carbon [36,37] and this is why substantial graphitization can be achieved even at a relatively low calcination temperature of 700 °C as used in this work. Furthermore, there were structural defects present in the graphitic domain, resulting in weak intensity diffraction peaks.[38] These structural defects are in fact beneficial for ion transport in electrochemical applications.

With the $Ni_3ZnC_{0.7}$/Ni composite nanocrystals removed, the final product loses its magnetic responsiveness and cannot be collected with a magnet, as demonstrated in Fig. S4b. Thermogravimetric analysis of the product in air was also conducted to further confirm the successful removal of the metallic components. From Fig. S5, it is evident that the sample weight dropped to zero after 550 °C, indicating the absence of $Ni_3ZnC_{0.7}$/Ni in the sample. If $Ni_3ZnC_{0.7}$/Ni remains in the sample, there will be formed corresponding oxides and the sample weight will be finite even at the high temperature of 550 °C.

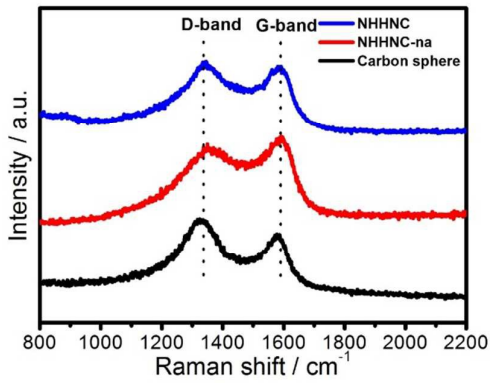

Fig. 3 Raman spectra of NHNNC, NHHNC-na, and carbon sphere

.

The graphitic and amorphous structures of the final product were further investigated with Raman spectroscopy. For comparison purposes, we prepared samples with procedures as those of the NHHNC but without the activation provided by the addition of $ZnCl_2$, termed NHHNC-na, and samples without the addition of $NiSO_4$, HMT, $ZnCl_2$, and HCl, termed carbon sphere. Fig. 3 shows the Raman spectra of all three samples. Two broad separate characteristic bands, D-band at 1346 cm^{-1} and G-band at 1590 cm^{-1}, were obtained. The D-band and G-band are generated from the defects present in the carbon structure and the in-plane vibrations of the graphitic structure, respectively. The intensity ratio of the D to G bands suggests the extent of graphitization achieved in the carbon material. A lower I_D/I_G value means a higher degree of graphitization.[39,40] The I_D/I_G values for the carbon sphere, NHHNC-na, and NHHNC are 1.2, 0.92, and 1.02, respectively. The I_D/I_G value is the highest for the carbon sphere, implying its lowest degree of graphitization. This is expected since the NHHNC and NHHNC-na samples both have the Ni formed in-situ to catalyze the graphitization of the carbon matrix. The NHHNC sample however showed a slightly lower graphitization degree, probably because of the less amount of Ni available for graphitization catalyzation than that of the NHHNC-na sample. Part of the Ni in the preparation of the NHHNC sample formed $Ni_3ZnC_{0.7}$ with Zn and C and did not participate in the catalyzation of carbon graphitization. On the contrary, for the preparation of the NHHNC-na sample, $ZnCl_2$ was not involved and thus no Ni was consumed for formation of $Ni_3ZnC_{0.7}$.

To further prove the successful N-doping and the detailed atomic environment of the nitrogen in the carbon materials, XPS measurements were conducted. The XPS survey spectra of the NHHNC-na and NHHNC samples are presented in Fig. 4a. Evidently, only C (285 eV), N (400 eV), and O (530 eV) are present

in the sample, with C as the dominant component and N and O as the minor components. Carbon came from the carbonization of the polysaccharide, nitrogen from the N-functional groups of the polysaccharide, and oxygen from the residual oxygen of the carbon skeleton.[41] The nitrogen contents were determined to be 8.05 and 6.87 at.% for the NHHNC-na and NHHNC samples, respectively. Fig. 4b and 4c show the detailed N1s spectra of the NHHNC-na and NHHNC samples, respectively. From peak de-convolution, one observes that there are four types of nitrogen containing groups present in the sample: pyridinic-N (N-6, 398.2 eV), pyrrolic-N (N-5, 399.9 eV), quaternary-N (N-Q, 400.8 eV), and pyridine-N-oxide (N-X, 402.4 eV).[42,43] A schematic was proposed in Fig. 4d to illustrate the four different types of atomic environment of the nitrogen in the carbon framework. From comparison of Fig. 4b and 4c, it is evident that the relative concentrations of N-6, N-5, and N-X decrease with the $ZnCl_2$ activation, while the relative concentration of N-4 increases. The combined relative concentration of N-5 and N-6 however is predominant in both samples. N-5 and N-6 have been shown to provide pseudo-capacitances and thus increase the specific capacitance of the electrode.[44,45] N-Q, on the other hand, is considered an in-graphene nitrogen substitution, which can improve the electric conductivity of the carbon material.[25,46] The N-doping is thus advantageous to boosting the capacitive performances of the electrode.

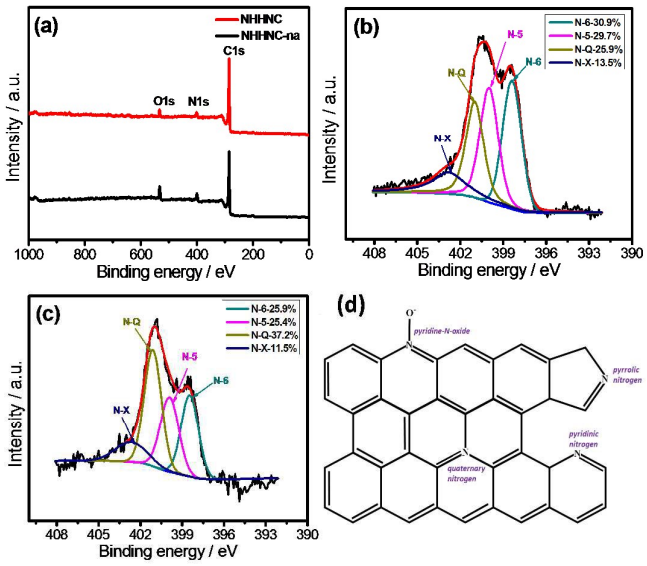

Fig. 4 XPS spectra of NHHNC and NHHNC-na: (a) survey spectra; (b) N1s spectrum of NHHNC; (c) N1s spectrum of NHHNC-na; (d) schematic illustration of various nitrogen functionalities identified by XPS.

The pore structure of the NHHNC-na and NHHNC samples was investigated next to study the effect of the $ZnCl_2$ activation on the capacitive performances of the two electrodes. The N_2 sorption/desorption isotherms of the two samples are depicted in Fig. 5a for comparison. Evidently, both samples gave type IV isotherms with H2 hysteresis loops at the P/P_0 range of 0.4-0.9, suggesting the existence of a large amount of mesopores in the samples.[47] This is confirmed by the pore size distributions shown in Fig. 5b, which reveal the bi-modal characteristic of the mesopore regime, with small mesopores centering at 4 nm and larger mesopores centering at 25 nm. The pore sizes are similar to those estimated from the HRTEM images. It can be conjectured that the smaller mesopores are mainly endowed by the structure defects of the graphite lattices, whereas the larger mesopores are ascribed to the voids created through etching removal of the $Ni_3ZnC_{0.7}$/Ni composite nanocrystals.[48] In addition, the adsorptions at the low P/P_0 region of the activated sample, NHHNC, are significantly higher than those of the non-activated sample, NHHNC-na, implying generation of a large amount of micropores through the $ZnCl_2$ activation.[49] Furthermore, the sharp increases in adsorption observed at the high P/P_0 region indicate the existence of macropores in the samples.[44,50] Consequently, one can conclude that the two samples possess not only mesopores but also micropores and macropores, and they are indeed hierarchical porous structure. The relevant pore structure parameters determined from analyses of the isotherms are summarized in Table 1. The specific Brunauer-Emmett-Teller (BET) surface areas were calculated to be 456 m^2 g^{-1} for the NHHNC-na sample and 707 m^2 g^{-1} for the NHHNC sample. The increase in specific surface area mainly came from the contribution of micropores, created from the $ZnCl_2$ activation, with the contribution fraction of the micropore increasing from 0.34 to 0.77. Similar for pore volumes, the micropore volume increased from 0.08 to 0.28 cm^3 g^{-1} with the activation. The average pore size of the NHHNC sample is 12.3 nm, significantly larger than 8.4 nm of the NHHNC-na sample, mainly because of the contribution of the bigger large mesopores as can be clearly seen from the pore size distribution curves. This would lead to smaller mass transfer resistances for ion transport in and out of the shell region of the hollow carbon structure, and thus beneficial for the high rate capability of the electrode. Also included in Table 1 for comparison are pore structure parameters obtained for the carbon spheres. For the carbon spheres, the specific surface area is only 361 m^2 g^{-1}, and the pores are mainly micropores, unlike the hierarchical pore structure of the NHHNC and NHHNC-na samples. Micropores alone, without the collaboration of mesopores and macropores, are detrimental to the ion transport involved in the capacitance generation processes. One thus expects poor capacitive performances for the carbon spheres.

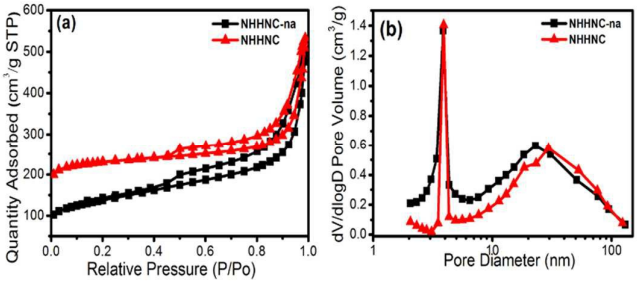

Fig. 5 (a) Nitrogen adsorption-desorption isotherms and (b) the pore size distribution curves of NHHNC and NHHNC-na.

Based on the above characterization results, one can conclude that the nest-like carbons are N-doped and partially graphitized, and possess hierarchical hollow porous structure of high specific surface areas. As proposed, both HMT and $NiSO_4$ play important roles in the formation of the N-doped hierarchical hollow nest-like carbon structure. HMT served not only as the precipitant, but also as the nitrogen source that reacted with the glucose to polymerize it into N-polysaccharide. For $NiSO_4$, it acted as the main structure-directing reagent for the formation of the nest-like structure, and also provided

Ni to serve as the catalyst for carbon graphitization during the carbonization process, and as the porogen for mesopore formation through an HCl etching. It is found that the N-doped hierarchical hollow nest-like carbon structure cannot be obtained without the participation of HMT or $NiSO_4$. Unlike the often cumbersome templating methods for fabrication of hierarchical porous carbon structures,[26,51] the present approach is novel, facile, and scalable, suitable for large scale production.

For the preparation of carbon materials, carbonization temperature is an important parameter and has great influences on the properties of the resulting carbon materials, such as specific surface areas, degree of graphitization, doping levels, etc. Generally speaking, the higher carbonization temperature, the higher degree of graphitization, but the lower specific surface areas and dopant contents. In the present work, Ni nanoparticles were formed through reduction of $Ni(OH)_2$ and served as a catalyst to graphitize amorphous carbon into graphitic carbon at low temperatures. In order to achieve a good combination of pore size, porosity, N-doping level, and degree of graphitization, we chose 700 ^oC as the carbonization temperature. Too low a carbonization temperature is unable to give sufficient graphitization to facilitate charge transport, whereas too high a carbonization temperature reduces the N-doping level and specific surface areas.

$ZnCl_2$ was introduced to facilitate the formation of micropores of the carbon sheets. The ratio of $ZnCl_2$ vs. the precursor, $Ni(OH)_2$@polysaccharide, thus has great influences on the specific surface area and morphology of the final product, NHHNC. On one hand, low dosages of $ZnCl_2$ cannot significantly increase the specific surface area of NHHNC. On the other hand, the morphology and porous structure of NHHNC would be damaged when the $ZnCl_2$ dosage is high because of the etching effect of $ZnCl_2$ on the carbon matrix. When the ratio of $ZnCl_2$ vs. precursor was increased up to 2:1 from 1:2, the morphology of the product was damaged after the HCl etching treatment as can be clearly seen through comparison of the SEM images, Fig. S6 and Fig. 1b, taken for the NHHNCs prepared from using the conditions of $ZnCl_2$ vs. precursor ratios of 2:1 and 1:2, respectively.

Table 1 Pore structure parameters of nitrogen-doped hierarchical nest-like carbons and carbon spheres.

Sample	S_{BET} (m^2 g^{-1})				Pore volume (cm^3 g^{-1})			D^b(nm)
	Total	Micro	Meso	Ratio[a]	Total	Micro	Meso	
NHHNC-na	456	157	299	0.34	0.78	0.08	0.70	8.4
NHHNC	707	543	164	0.77	0.82	0.28	0.54	12.3
Carbon sphere	361	324	37	0.90	0.19	0.17	0.02	1.2

a: ratio of micropore area to total area.
b: average pore diameter.

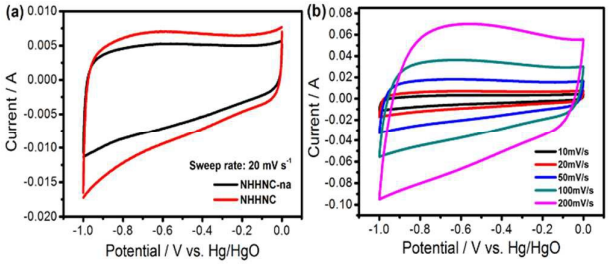

Fig. 6 Cyclic voltammetry curves of (a) NHHNC-na and NHHNC at scan rate of 20 mV s^{-1} and (b) NHHNC electrode at increasing scan rates.

The capacitive performances of the nitrogen-doped hierarchical hollow nest-like carbon structures were evaluated with both cyclic voltammetry (CV) and galvanostatic charging/discharging measurements. Fig. 6a shows the CVs of the NHHNC-na and NHHNC electrodes recorded at a scan rate of 10 mV s^{-1}. Both CVs appear quite rectangular with a pair of broad redox peaks, centering at -0.7 and -0.6 V. This indicates that both electrical double-layer capacitances and pseudo-capacitances were generated from the electrodes. The pseudo-capacitances may be ascribed to the redox reactions between the N-carrying functional groups of the carbon sheet with the electrolyte ions.[52] The following redox reactions have been proposed:[53]

$$C^*\text{-}NH_2 + 2OH^- \rightleftharpoons C^*\text{-}NHOH + H_2O + 2e^- \quad (4)$$

$$C^*H\text{-}NH_2 + 2OH^- \rightleftharpoons C^*{=}NH + 2H_2O + 2e^- \quad (5)$$

From Fig. 6a, it is evident that the NHHNC electrode achieved larger capacitive currents and thus higher capacitances than those of the NHHNC-na electrode. This may be attributed to the significantly larger specific surface area of the NHHNC electrode, acquired through the $ZnCl_2$ activation, for accommodation of larger amounts of EDLCs. Fig. 6b shows the CVs of the NHHNC electrode recorded at increasing scan rates from 10 to 200 mV s^{-1}. The capacitive currents increase with increasing scan rate as expected, with the quasi-rectangular shape well retained even at the high scan rate of 200 mV s^{-1}. As for the NHHNC-na electrode, the shape of the CVs turns increasingly more skewed with increasing scan rate (Fig. S7a). As for the carbon sphere electrode, the shape of the recorded CVs deviated severely from the ideal rectangular shape (Fig. S8a) and the situation turned worse with increasing scan rates. The differences between the three electrodes in high rate performance may be roughly attributed to the pore size of the electrode material. The NHHNC electrode, with the largest average pore size, experienced the least mass transfer resistances, among the three, in the capacitance generation process, and thus the best high rate capability performance.

To further investigate the capacitive performances of the three electrodes, galvanostatic charge/discharge (C/D) measurements were conducted at increasing current densities. Fig. 7a shows the C/D curves of the NHHNC electrode at increasing charge/discharge current densities from 1 to 20 A g^{-1}. All C/D curves appear nearly triangular without apparent iR drops, indicating small internal resistances, attributable to the good electric conductivities and low mass transfer resistances enabled by the N-doping, partial graphitization, and hierarchical hollow structure of the NHHNC electrode.[54] The curves however are not strictly symmetrical especially at low current densities, with the discharging curve showing slight tailing. This phenomenon has been observed and reported for N-doped carbon electrodes.[17,25,55]

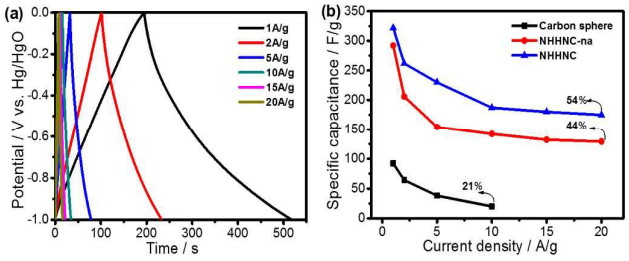

Fig. 7 (a) Galvanostatic charge/discharge curves of NHHNC at increasing current densities. (b) Variation of specific capacitance with increasing current densities for all three samples.

The specific capacitance can be calculated according to the formula $C=It/m\Delta V$, where I is the charge/discharge current, t the discharge time, m the mass of the active material, and ΔV the operation potential window. Fig. 7b shows the specific capacitance as a function of increasing current densities for the NHHNC and NHHNC-na electrodes to evaluate their high rate capability. The NHHNC electrode consistently outperformed the NHHNC-na electrode in specific capacitance at all current densities. The specific capacitances of the NHHNC electrode are 322, 262, 230, 187, 180, and 175 F g^{-1} as determined at current densities of 1, 2, 5, 10, 15, and 20 A g^{-1}, respectively. It is worth mentioning that the high specific capacitance of 322 F g^{-1} achieved by the NHHNC electrode in 6 M KOH is higher than those of most N-doped carbon materials previously reported in literature, including graphene,[15,54] 3-D porous carbons,[56] carbon nanotubes,[57] carbon nanocages,[58] ordered mesoporous carbon,[59] and carbon nanofibers[18] A more detailed comparison is compiled in Table 2.

Furthermore, the high rate capability of the NHHNC electrode also outperformed that of the NHHNC-na electrode. The specific capacitance retention achieved by the NHHNC electrode was 54% at 20 A g^{-1} taking that at 1 A g^{-1} as the basis. The specific capacitance retention for the NHHNC-na electrode was only 44% under the same testing condition. As for the carbon sphere electrode, as expected for poor capacitive performances, its specific capacitance was only92 F g^{-1} at1 A g^{-1} and dramatically dropped to 20 F g^{-1} at 10 A g^{-1}, giving a specific capacitance retention rate of only 21%. The excellent high rate capability of the NHHNC electrode may be attributed to its open and interconnected three-dimensional hierarchical

Table 2. Comparison of specific capacitances of representative nitrogen-doped carbon materials in 6 M KOH compiled from literature

Materials	S_{BET} (m^2 g^{-1})	N %	Current density (A g^{-1})	C_g (F g^{-1})	Ref.
nitrogen-doped graphene hydrogels	1521	5.86	3	308	15
nitrogen-doped porous nanofibers	562.5	7.22	1.0	202	18
graphene-incorporated nitrogen-rich carbon composite	1646	2.2	0.1	300	54
3D nitrogen-doped porous carbon	1470	8.2	0.5	296	56
porous nitrogen-doped carbon nanotube	1765	4.56	0.5	210	57
nitrogen-doped graphitic carbon nanocage	1001	8.3	1.0	248	58
nitrogen-doped ordered mesoporous carbon	537	13.1	0.2	227	59
NHHNC	707	6.87	1.0	322	This work

hollow structure. The large amount of surface micropores provides abundant surface areas to accommodate electric double layers and electroactive N-doped sites to generate pseudocapacitances. The macropores served as an ion-buffering reservoir that shortened the electrolyte diffusion distances, lessening the mass transfer resistances for better high rate capability.[22] More importantly, the partially graphitized carbon sheets facilitated the fast electron transport between the active material and the current collector, thus also enhancing the kinetic performance of the electrode.

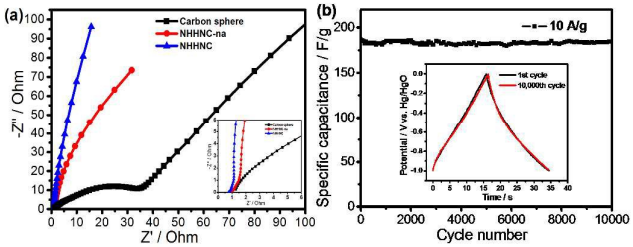

Fig. 8 (a) Nyquist plots of all three samples. Inset shows locally enlarged Nyquist plots in high frequency region. (b) Specific capacitance of NHHNC electrode for 10,000-cycle charge/discharge test at current densities of 10 A g^{-1}. Inset shows galvanostatic charge/discharge curves of NHHNC electrode at current densities of 10 A g^{-1} at 1st and 10,000th cycles.

The electrode kinetic characteristics of the electrodes were further studied with electrochemical impedance spectroscopy (EIS). Fig. 8a shows the Nyquist plots recorded for the three electrodes. The plots exhibit two feature regions, a line obtained at low frequencies and a semi-arc formed at high frequencies. The low frequency line and the high frequency semi-arc characterized the diffusion resistance of the electrolyte ions and reflected the charge transport resistance, respectively. The steeper the line, the lower the diffusion resistance, and the smaller the semi-arc, the lower the charge transport resistance. Not surprisingly, the carbon sphere electrode gave an inclined line at the low-frequency region, indicating poor capacitive performance and high ion-diffusion resistances. On the other hand, the NHHNC electrode gave a near vertical line at low frequencies, and the slope of the near vertical line is significantly larger than that of the NHHNC-na electrode. This may be attributed to the higher specific surface area and larger average pore size of the NHHNC electrode achieved with the $ZnCl_2$ activation. These two structural features provide better accessibility and thus more effective exposure of active sites to the electrolyte, even at high current densities. In addition, the semi-arc of the carbon sphere electrode is much larger than those of the NHHNC-na and NHHNC electrodes, implying the poor charge conductivity of the

carbon sphere electrode. Recall that the nickel formed in-situ during the carbonization process can catalyze the graphitization of the carbon network and thus improve the electric conductivities of the electrode. Note that the EIS results are in good agreement with those of the CV and C/D measurements, further confirming that the NHHNC electrode possesses both low ion transport and low charge transport resistances.

Excellent cycling stability is also an essential requirement for the practical application of supercapacitors. Fig. 8b shows the specific capacitance *vs.* cycle number for the NHHNC electrode. The electrode exhibited an excellent cycling stability, with only 2% loss in specific capacitance after 10,000 cycles at a current density of 10 A g^{-1}. Additionally, the almost ideal triangular charge/discharge curves remained almost unchanged after 10,000 cycle operations, as shown in the inset of the figure, confirming again the outstanding cycling stability of the electrode.

4. Conclusions

In summary, we have successfully developed a novel facile, scalable template-free method to fabricate N-doped hierarchical hollow nest-like carbon structure. The unique and advantageous structural features of this product, together with the fast charge transport ability of the partially graphitized carbon sheets and extra pseudo-capacitances generated through superficial redox reactions of the N-doped sites, led to a successful application as the electrode material for supercapacitors. The NHHNC electrode exhibited a high specific capacitance of 322 F g^{-1} at 1 A g^{-1}, an excellent high rate capability of 54% capacitance retention at 20 A g^{-1}, and an outstanding cycling stability of only 2% loss in specific capacitance after 10,000 cycles at a current density of 10 A g^{-1}, among the best reported. The present template-free process however, unlike the often cumbersome templating ones, is well suited for large scale production and thus practical applications. Furthermore, this unique hierarchical hollow nest-like carbon structure, because of its advantageous structural features, can be applied to a wide variety of applications, including energy storage, catalyst supports, adsorption media, and chromatographic separation systems.

Acknowledgements

This work was financially supported by the Ministry of Science and Technology of Taiwan under grant MOST 103-2221-E-007-119-MY2, and by the Top Program and Low Carbon Energy Research Center of the National Tsing Hua University.

Notes and references

1. P. Simon and Y. Gogotsi, *Nat. Mater.*, 2008, **7**, 845-854.
2. Y. Zhu, S. Murali, M. D. Stoller, K. J. Ganesh, W. Cai, P. J. Ferreira, A. Pirkle, R. M. Wallace, K. A. Cychosz, M. Thommes, D. Su, E. A. Stach and R. S. Ruoff, *Science*, 2011, **332**, 1537-1541.
3. G. Wang, L. Zhang and J. Zhang, *Chem. Soc. Rev.*, 2012, **41**, 797-828.
4. M. M. Titirici, R. J. White, N. Brun, V. L. Budarin, D. S. Su, F. del Monte, J. H. Clark and M. J. MacLachlan, *Chem. Soc. Rev.*, 2015, **44**, 250-290.
5. H. C. Chien, W. Y. Cheng, Y. H. Wang and S. Y. Lu, *Adv. Funct. Mater.*, 2012, **22**, 5038-5043.
6. L. L. Zhang and X. S. Zhao, *Chem. Soc. Rev.*, 2009, **38**, 2520-2531.
7. W. T. Gu, M. Sevilla, A. Magasinski, A. B. Fuertes and G. Yushin, *Energy Environ. Sci.*, 2013, **6**, 2465-2476.
8. Z. S. Wu, A. Winter, L. Chen, Y. Sun, A. Turchanin, X. Feng and K. Mullen, *Adv. Mater.*, 2012, **24**, 5130-5135.
9. F. B. Su, C. K. Poh, J. S. Chen, G. W. Xu, D. Wang, Q. Li, J. Y. Lin and X. W. Lou, *Energy Environ. Sci.*, 2011, **4**, 717-724.
10. D. M. Anjos, J. K. McDonough, E. Perre, G. M. Brown, S. H. Overbury, Y. Gogotsi and V. Presser, *Nano Energy*, 2013, **2**, 702-712.
11. D. Hulicova‐Jurcakova, M. Seredych, G. Q. Lu and T. J. Bandosz, *Adv. Funct. Mater.*, 2009, **19**, 438-447.
12. J. P. Paraknowitsch and A. Thomas, *Energy Environ. Sci.*, 2013, **6**, 2839-2855.
13. K. N. Wood, R. O'Hayre and S. Pylypenko, *Energy Environ. Sci.*, 2014, **7**, 1212-1249.
14. B. Xu, H. Duan, M. Chu, G. P. Cao and Y. S. Yang, *J. Mater. Chem. A*, 2013, **1**, 4565-4570.
15. H. L. Guo, P. Su, X. F. Kang and S. K. Ning, *J. Mater. Chem. A*, 2013, **1**, 2248-2255.
16. K. Jost, D. Stenger, C. R. Perez, J. K. McDonough, K. Lian, Y. Gogotsi and G. Dion, *Energy Environ. Sci.*, 2013, **6**, 2698-2705.
17. J. P. Han, G. Y. Xu, B. Ding, J. Pan, H. Dou and D. R. MacFarlane, *J. Mater. Chem. A*, 2014, **2**, 5352-5357.
18. L. F. Chen, X. D. Zhang, H. W. Liang, M. G. Kong, Q. F. Guan, P. Chen, Z. Y. Wu and S. H. Yu, *ACS Nano*, 2012, **6**, 7092-7102.
19. J. H. Lee, N. Park, B. G. Kim, D. S. Jung, K. Im, J. Hur and J. W. Choi, *ACS Nano*, 2013, **7**, 9366-9374.
20. M. Sevilla and A. B. Fuertes, *ACS Nano*, 2014, **8**, 5069-5078.
21. L. Zhu, H.-J. Peng, J. Liang, J.-Q. Huang, C.-M. Chen, X. Guo, W. Zhu, P. Li and Q. Zhang, *Nano Energy*, 2015, **11**, 746-755.
22. D. W. Wang, F. Li, M. Liu, G. Q. Lu and H. M. Cheng, *Angew. Chem., Int. Ed.*, 2008, **47**, 373-376.
23. Y. Li, Z. Li and P. K. Shen, *Adv. Mater.*, 2013, **25**, 2474-2480.
24. Z. N. Yu, L. Tetard, L. Zhai and J. Thomas, *Energy Environ. Sci.*, 2015, **8**, 702-730.
25. S. Zhong, C. X. Zhan and D. P. Cao, *Carbon*, 2015, **85**, 51-59.
26. Q. Wang, J. Yan, Y. B. Wang, T. Wei, M. L. Zhang, X. Y. Jing and Z. J. Fan, *Carbon*, 2014, **67**, 119-127.
27. G. A. Ferrero, A. B. Fuertes and M. Sevilla, *J. Mater. Chem. A*, 2015, **3**, 2914-2923.
28. B. Fang, J. H. Kim, M.-S. Kim and J.-S. Yu, *Acc. Chem. Res.*, 2012, **46**, 1397-1406.
29. X. Wen, D. Zhang, L. Shi, T. Yan, H. Wang and J. Zhang, *J. Mater. Chem.*, 2012, **22**, 23835-23844.
30. L. Wang, G. Mu, C. Tian, L. Sun, W. Zhou, P. Yu, J. Yin and H. Fu, *ChemSusChem*, 2013, **6**, 880-889.
31. J. H. Kim, D. Bhattacharjya and J.-S. Yu, *J. Mater. Chem. A*, 2014, **2**, 11472-11479.
32. M. Gruzdev, U. Chervonova, A. Kolker and N. Domracheva, *J. Struct. Chem.*, 2011, **52**, 83-90.
33. X. G. Zheng, H. L. Wang, Q. Gong, L. C. Zhang, G. L. Cui, Q. S. Li, L. Chen, F. Q. Wu and S. M. Wang, *Mater. Lett.*, 2015, **143**, 290-293.
34. C. Falco, M. Sevilla, R. J. White, R. Rothe and M. M. Titirici, *ChemSusChem*, 2012, **5**, 1834-1840.
35. A. Alabadi, X. J. Yang, Z. H. Dong, Z. Li and B. E. Tan, *J. Mater. Chem. A*, 2014, **2**, 11697-11705.
36. J. Y. Liang, S. L. Chen, M. J. Xie, Y. Z. Wang, X. K. Guo, X. F. Guo and W. P. Ding, *J. Mater. Chem. A*, 2014, **2**, 16884-16891.
37. S. M. Yoon, W. M. Choi, H. Baik, H. J. Shin, I. Song, M. S. Kwon, J. J. Bae, H. Kim, Y. H. Lee and J. Y. Choi, *ACS Nano*, 2012, **6**, 6803-6811.
38. J. S. Lee, S. I. Kim, J. C. Yoon and J. H. Jang, *ACS Nano*, 2013, **7**, 6047-6055.
39. D. D. Li, L. X. Ding, H. B. Chen, S. Q. Wang, Z. Li, M. Zhu and H. H. Wang, *J. Mater. Chem. A*, 2014, **2**, 16617-16622.
40. P. Hao, Z. Zhao, J. Tian, H. Li, Y. Sang, G. Yu, H. Cai, H. Liu, C. P. Wong and A. Umar, *Nanoscale*, 2014, **6**, 12120-12129.
41. S. Chen, J. Duan, M. Jaroniec and S. Z. Qiao, *Adv. Mater.*, 2014, **26**, 2925-2930.
42. G. Lota, B. Grzyb, H. Machnikowska, J. Machnikowski and E. Frackowiak, *Chem. Phys. Lett.*, 2005, **404**, 53-58.
43. Y. T. Hu, H. J. Liu, Q. Q. Ke and J. Wang, *J. Mater. Chem. A*, 2014, **2**, 11753-11758.
44. L. Wan, J. Wang, L. Xie, Y. Sun and K. Li, *ACS Appl. Mater. Interfaces*, 2014, **6**, 15583-15596.

45. C. O. Ania, V. Khomenko, E. Raymundo-Pinero, J. B. Parra and F. Beguin, *Adv. Funct. Mater.*, 2007, **17**, 1828-1836.
46. L. Sun, C. Tian, Y. Fu, Y. Yang, J. Yin, L. Wang and H. Fu, *Chem. Eur. J.*, 2014, **20**, 564-574.
47. Z. J. Fan, Y. Liu, J. Yan, G. Q. Ning, Q. Wang, T. Wei, L. J. Zhi and F. Wei, *Adv. Energy Mater.*, 2012, **2**, 419-424.
48. H.-J. Peng, J. Liang, L. Zhu, J.-Q. Huang, X.-B. Cheng, X. Guo, W. Ding, W. Zhu and Q. Zhang, *ACS Nano*, 2014, **8**, 11280-11289.
49. Q. Wang, Q. Cao, X. Y. Wang, B. Jing, H. Kuang and L. Zhou, *J. Power Sources*, 2013, **225**, 101-107.
50. Y. Mun, C. Jo, T. Hyeon, J. Lee, K.-S. Ha, K.-W. Jun, S.-H. Lee, S.-W. Hong, H. I. Lee and S. Yoon, *Carbon*, 2013, **64**, 391-402.
51. X. Y. Chen, Y. Y. He, Y. K. Xia and Z. J. Zhang, *J. Mater. Chem. A*, 2014, **2**, 17586-17594.
52. L. Qie, W. M. Chen, H. H. Xu, X. Q. Xiong, Y. Jiang, F. Zou, X. L. Hu, Y. Xin, Z. L. Zhang and Y. H. Huang, *Energy Environ. Sci.*, 2013, **6**, 2497-2504.
53. B. Xu, S. Hou, G. Cao, F. Wu and Y. Yang, *J. Mater. Chem.*, 2012, **22**, 19088-19093.
54. X. Fan, C. Yu, J. Yang, Z. Ling and J. Qiu, *Carbon*, 2014, **70**, 130-141.
55. B. You, L. Wang, L. Yao and J. Yang, *Chem. Commun.*, 2013, **49**, 5016-5018.
56. J. Pu, C. Li, L. Tang, T. Li, L. Ling, K. Zhang, Y. Xu, Q. Li and Y. Yao, *Carbon*, 2015, **94**, 650-660.
57. G. Xu, B. Ding, P. Nie, L. Shen, J. Wang and X. Zhang, *Chem. Eur. J.*, 2013, **19**, 12306-12312.
58. Y. Tan, C. Xu, G. Chen, Z. Liu, M. Ma, Q. Xie, N. Zheng and S. Yao, *ACS Appl. Mater. Interfaces*, 2013, **5**, 2241-2248.
59. J. Wei, D. Zhou, Z. Sun, Y. Deng, Y. Xia and D. Zhao, *Adv. Funct. Mater.*, 2013, **23**, 2322-2328.

Glucose-derived nitrogen-doped hierarchical hollow nest-like carbon nanostructure from a novel template-free method as an outstanding electrode material for supercapacitors

Ji-Yuan Liang, Chun-Chieh Wang, Shih-Yuan Lu*

Received (in XXX, XXX) Xth XXXXXXXXX 20XX, Accepted Xth XXXXXXXXX 20XX
DOI: 10.1039/b000000x

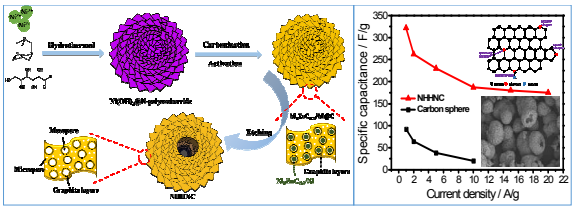

Nitrogen-doped hierarchical hollow nest-like carbon nanostructure, fabricated from glucose with a novel template-free method, exhibited outstanding supercapacitive performances.